Combustion and Flame 160 (2013) 1990–1998

Contents lists available at SciVerse ScienceDirect

Combustion and Flame

journal homepage: www.elsevier.com/locate/combustflame

Comparison of structures of laminar methane–oxygen and methane–air diffusion flames from atmospheric to 60 atm

Peter H. Joo, Marc R.J. Charest, Clinton P.T. Groth, Ömer L. Gülder *

University of Toronto, Institute for Aerospace Studies, 4925 Dufferin Street, Toronto, Ontario, Canada M3H 5T6

ARTICLE INFO

Article history:
Received 16 November 2012
Received in revised form 26 March 2013
Accepted 30 April 2013
Available online 5 June 2013

Keywords:
Oxy-fuel combustion
Methane–oxygen flames
High pressure diffusion flames
Soot formation at high pressures
Two zone flame structure

ABSTRACT

A combined experimental and numerical study was conducted to examine the structure of laminar methane–oxygen diffusion flames in comparison with methane–air flames. Soot measurements made in these flames indicated that the maximum soot yields of methane–air flames are consistently higher than methane–oxygen flames at all pressures. The maximum soot yield of the methane–oxygen flames reaches a peak near 40 atm and then starts decreasing as the pressure further increased. The maximum soot yield of the methane–air flames plateaus at about 40 atm and does not change much with further increases in pressure. Methane–oxygen flames display a distinct two-zone structure which is visible from atmospheric pressure up to 60 atm. The inner zone, similar to hydrocarbon-air diffusion flames, has a yellow/orange colour and is surrounded by an outer blue zone. This outer zone was shown to have a stratified structure with a very steep equivalence ratio gradient. The main reactions in this zone were shown to be the oxidation of hydrogen and carbon monoxide produced within the inner zone. The methane–air diffusion flames had a thin layer of blue outer zone at atmospheric pressure; however, this zone completely disappeared when the pressure was increased above atmospheric. The presence of the two-zone structure in the methane–oxygen flames was attributed to the intensified penetration of oxygen into the core flow. The higher diffusivities, steeper oxygen concentration gradients, and enhanced entrainment increase the transport of oxygen to the flame. As such, there is sufficient oxygen present near the base of the flame to support the diffusion flame in the inner zone of the methane–oxygen flames. The abundance of oxygen near the centerline, even in the lower portion of the flame, also promotes the oxidation of soot.

1. Introduction

Soot formation, and to a certain extent soot oxidation, in laminar diffusion flames of hydrocarbon fuels is dependent on several parameters which ultimately determine the overall soot yield of a flame. These parameters include: the chemical structure of the fuel [1–5], the temperature of the flame [6], the presence of diluents or additives in the fuel and/or air stream [7–10], and the pressure [4,11–13].

Typical combustion devices used in air- and land-based transportation vehicles, as well as those used in stationary power generation, operate at pressures well above atmospheric. For example, pressures in current aviation gas turbines approach 40 atm whereas pressures in the combustion chamber of a liquid propellant rocket engine may reach up to 200 atm. These operating pressures are well above the critical pressures of common hydrocarbon fuels and air. In spite of this fact, our understanding of high pressure combustion and its governing mechanisms is limited when compared with our understanding of combustion under atmospheric conditions. Although there have been efforts to project the combustion data obtained at atmospheric conditions to elevated pressures, there is no reliable method to perform this projection. For example, combustion intensity, i.e., energy release per unit volume, scales with the square of pressure while the soot yield in diffusion flames has a much more complex relationship with pressure that depends on pressure itself [13]. Thus, the influence of pressure on combustion is not trivial.

One evolving area of research is combustion involving pure oxygen (or highly oxygen enriched air) as the oxidizing agent, called oxy-fuel combustion. Oxy-fuel combustion is a promising enabling technology for zero-emission combustion devices that capture carbon dioxide and it may also be of great benefit for use in rocket engines. In comparison to conventional combustion using air, oxy-fuel combustion offers a number of technical advantages in terms of thermal efficiency, combustion stability, enhanced heat transfer, and emissions control [14–16]. However, due to the high flame temperatures that occur during oxy-fuel combustion, diluents such as carbon dioxide or steam must be used for flame temperature

* Corresponding author. Address: University of Toronto, UTIAS, 4925 Dufferin Street, Toronto, Ontario, Canada M3H 5T6. Fax: +1 416 667 7799.
E-mail address: ogulder@utias.utoronto.ca (Ö.L. Gülder).

0010-2180/$ - see front matter © 2013 The Combustion Institute. Published by Elsevier Inc. All rights reserved.
http://dx.doi.org/10.1016/j.combustflame.2013.04.030

control and material cooling. This makes its successful application difficult.

In terms of rocket propulsion, liquid oxygen-hydrocarbon engine systems offer significant advantages for future launch vehicles, such as favorable cost, better reliability, simpler ground operation, reduced overall mass of the vehicle and improved mission flexibility. Most importantly, they offer reduced operational costs and smaller propellant tank sizes when compared with liquid oxygen-hydrogen systems, which is especially advantageous for booster or core stage engines. Liquid oxygen-kerosene and liquid oxygen-methane systems seem to be the most likely candidates. Recently there has been considerable interest in the potential use of methane and liquid oxygen as propellants for reusable rocket engines [17]. Liquid oxygen-methane is viewed as one of the most promising propellant combinations [17].

A few studies exist that involve methane and liquid oxygen combustion with the aim of reproducing conditions relevant to rocket applications, i.e., turbulent conditions and supercritical methane pressures. But the complexities introduced by turbulence make it difficult to fully characterize the highly-coupled interaction between physical processes that occurs during oxy-fuel combustion. Therefore, studies of oxy-fuel combustion involving simpler laminar diffusion flames, from which the results can be applied to turbulent flames, are necessary to expand our fundamental understanding of such processes. Unfortunately, information on the structure and characteristics of laminar diffusion flames of methane and oxygen is limited. Most of the research related to oxy-fuel combustion applications was performed at atmospheric pressures using oxygen enriched air for the oxidizer. Sugiyama [7] and Lee et al. [8] reported the effects of oxygen concentration in the air stream on soot formation in laminar co-flow diffusion flames of methane at atmospheric conditions. Sugiyama [7] suggested that the reduced soot concentrations with increasing co-flow oxygen concentration in acetylene flames was due to changes in velocity field and flame shape. Lee et al. [8] reported that the soot surface growth and oxidation rates are higher in flames of methane with an oxidizer consisting of 50% oxygen and 50% nitrogen as compared to the rates in a methane–air base flame. They also found that as the oxygen concentration is increased in the oxidizer flow, soot volume fractions in the flame are decreased [8]. Du et al. [9] reported that the effect of oxygen concentration on the oxidizer side of ethylene and propane counter-flow diffusion flames is almost totally thermal. In a more recent numerical study of a counter-flow flame of liquid oxygen and methane at transcritical conditions, species concentrations and temperature profiles were calculated at 70 atm for three scenarios of liquid oxygen and methane injection temperatures [18]. It is well known that liquefied methane has favorable cooling characteristics that can be used in combustion chambers with regenerative cooling [19,20].

Most recently, measurements were obtained for soot volume fraction and temperature in laminar methane–oxygen co-flow flames at elevated pressures between 10 and 90 atm [21]. Two distinct zones were observed in the visual appearance of the flames: an inner luminous zone similar to methane–air diffusion flames and an outer diffusion flame zone which was mostly blue. With the aid of numerical analysis, it was concluded that the blue flame zone starts as a diffusion flame of hydrogen and carbon monoxide burning in oxygen and turns into a partially premixed flame as a result of intense penetration of oxygen into the flame zone. The measurements revealed an unexpected relationship between soot yield and pressure. The overall soot yield increased with pressure between 10 and 40 atm, but decreased when pressure was increased further above 40 atm.

In the current work, the experimental measurements and numerical results initially reported by Joo and Gülder [21] were analyzed further. The two-zone structure of the laminar methane–oxygen diffusion flames, observed experimentally at atmospheric and elevated pressures, was studied and compared to the structure of methane–air diffusion flames. New measurements of soot volume fractions for methane–air flames at flow rates similar to those for the methane–oxygen flames were obtained and discussed. Additionally, predictions of species concentration, temperature and velocity distributions were investigated to expand on the observed changes in physical appearance between the air and oxygen flames. Previously, only the predicted temperature and concentrations for several species along the centerline were reported by Joo and Gülder [21] for these flames.

2. Experimental details

Experiments were conducted in a combustion chamber capable of operating at sub- and super-atmospheric pressures with an inner diameter of 0.24 m and a height of 0.60 m. Inside, the fuel nozzle of the burner is 3 mm in diameter and the co-flow air nozzle has a diameter of 25 mm. The details of the combustion chamber and the laminar co-flow diffusion flame burner used in this study have already been described in more detail [22–24]. A schematic of the experimental set-up is shown in Fig. 1. The thermal-based mass flow meter is calibrated for low and high pressure uses and has a maximum total error of less than 2%.

A non-intrusive, line-of-sight spectral soot emission (SSE) diagnostic technique was used to obtain the temperature and the soot volume fraction. In the SSE diagnostic, line-of-sight radiation emissions from soot are measured along chords through the flame at a given height. Soot emission is measured over the wavelength range of 690–945 nm. Spectra are averaged over the height of the entrance slit as well as across twelve spectral regions, each 21 nm wide. This provides 12 adjacent spectral data points per line-of-sight acquisition. Output from the spectrometer is focused onto a calibrated 16-bit CCD detector (1100×330 pixels). The lateral emission scans are inverted to obtain radially resolved emission data using the three-point Abel deconvolution technique, after which temperature and soot volume fraction can be determined since soot optical properties are known [25]. Soot radiation emissions are measured every 50 μm across the flame at the height increments of 0.5 mm. Details of the theory are provided elsewhere [26] and the specifics of the overall experimental layout of the

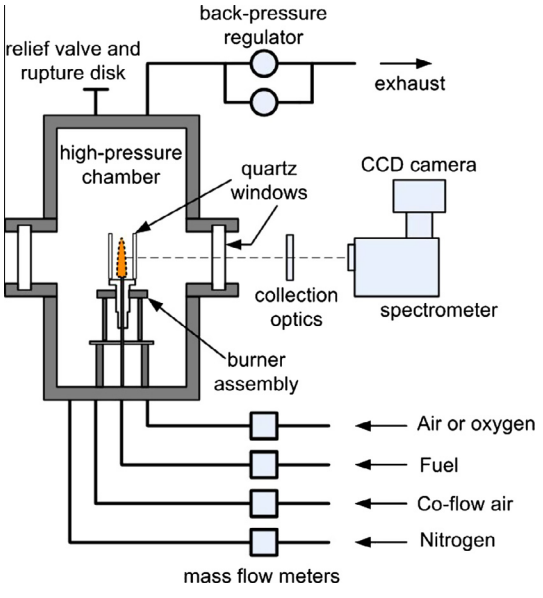

Fig. 1. A schematic view of the experimental setup.

spectral soot emission diagnostic used in this study are provided by Joo and Gülder [24].

Schalla et al. [11,12] showed that the reciprocal of the smoke point fuel mass flow rate scales with pressure approximately as $P^{1.0\pm0.2}$ for a range of fuels in air at pressures up to 12 atm [12]. Flower and Bowman [27] obtained a similar relationship in experiments for high-pressure ethylene-air flames. They found the reciprocal of the smoke point fuel mass flow rate scaled with $P^{1.3}$. Therefore, the fuel mass flow rate should be kept constant during high pressure diffusion flame soot experiments in order to allow direct comparisons [13,28]. Additionally, the fuel mass flow rate should be determined at the highest planned pressure since soot yield is known to increase with pressure [13]. Otherwise the smoke point will be reached during the experiments, which would significantly complicate the analysis of soot formation and oxidation. Residence times and temperatures in smoking flames are difficult to define and measure [13].

The methane flow rate for the experiments of Joo and Gülder [21] were originally selected to be 1.1 mg/s. With this flow rate, the methane–oxygen flames were very stable at all pressures up to 60 atm. Methane–air flames with a 1.1 mg/s flow rate, however, were highly unstable at pressures above a few atmospheres and began to smoke. Reducing the flow rate to 0.825 mg/s provided stable, non-smoking flames up to 20 atm, which is the same flow rate for similar flames studied by Gülder et al. [29]. Joo and Gülder [24] were able to obtain stable, non-smoking methane–air flames at pressures up to 60 atm with methane flow rates of 0.55 mg/s. However, Joo and Gülder [21] could not obtain measurements in methane–oxygen flames with a methane flow rate of 0.55 mg/s above 10–15 atm due to very small flame sizes and solid carbon deposition on the burner rim. As a result, the methane–air and methane–oxygen flames were studied over a range of pressures and flow rates, which are listed in Table 1. Some of the experimental data for the methane–oxygen and methane–air flames were reported previously in [21,24,29].

3. Numerical approach

The present study expands upon the initial numerical analysis performed by Joo and Gülder [21]. In their study and ours, the numerical comparison between the flame structures of methane–oxygen and methane–air flames was performed under atmospheric conditions only. The study makes use of a previously developed framework for modeling laminar reactive flows with complex chemistry, non-gray radiative heat transfer and soot [30] which has been used previously in a number of studies of laminar flames under both high-pressure and micro-gravity conditions [31–33]. This framework describes gaseous combusting flow using the conservation equations for continuous, multi-component compressible gas mixtures [34]. The equations consist of the conservation of total mixture mass, individual species mass, mixture momentum, and mixture energy. Soot formation/oxidation and radiation were not included here since their effects are expected to be relatively small at atmospheric pressure.

Table 1
Fuel mass flow rates and the pressure ranges of the previous measurements and the current data.

Oxidizer	Methane flow rate (mg/s)	Pressure range (atm)	Source
Air	1.1	1–5	This work
	0.825	1–20	[45]
	0.55	1–60	[24]
Oxygen	1.1	1–60	[21]
	0.55	1	[21]

The equations governing the gas mixture are solved numerically using a parallel, block-based, adaptive mesh refinement (AMR), finite-volume scheme on body-fitted, multi-block quadrilateral mesh previously developed by Groth and co-workers [30,35–40]. The scheme makes use of piecewise limited linear reconstruction and an approximate Riemann solver to determine the inviscid fluxes [40]. The second-order diamond-path method developed by Coirier and Powell [41] is used to compute the viscous fluxes. Both the inviscid flux and the temporal derivative are preconditioned using the proposed matrix of Weiss and Smith [42]. This preconditioning helps reduce excessive dissipation and numerical stiffness commonly encountered when applying the compressible gas equations to low-Mach-number flows. The solution of the fully-coupled nonlinear ODEs are relaxed to a steady-state using the block-based parallel implicit algorithm developed by Northrup and Groth [30,37] which makes use of a matrix-free inexact Newton–Krylov method. As noted above, this framework has been previously and successfully applied to the studies on the effects of pressure and gravity on laminar co-flow methane and ethylene diffusion flames [31–33].

Thermodynamic and transport properties along with gas-phase kinetic rates are all evaluated in the solution method described above using CANTERA [43], an open-source software package for chemically-reacting flows. The simulations were performed using a modified version of the Gri-Mech 3.0 mechanism for methane combustion [44]. Nitrogen was assumed to be inert and all reactions and species related to NOx formation were removed from the mechanism, giving a final reduced mechanism with 36 species and 219 reactions.

4. Results and discussion

4.1. Initial observations

Joo and Gülder [21] observed that atmospheric methane–oxygen diffusion flames had a two zone structure that appeared to persist at elevated pressures. The inner zone, zone I, is similar to a laminar methane–air flame, luminous and mostly yellow/orange in color. This inner zone is surrounded by an outer zone, zone II, which is mostly blue and occupies a larger volume of the flame. Figure 2 compares still images of the methane–oxygen and methane–air flames over a range of pressures. At atmospheric pressure, we observed a similar blue flame surrounding the luminous zone in methane–air flames, as shown in Fig. 2b. However, this thin blue layer disappeared as soon as the pressure was increased to above atmospheric. Saito et al. [45] also noticed a very thin layer of a blue flame enclosing the yellow luminous zone of atmospheric methane–air diffusion flames at low methane flow rates.

It should be noted here that for a similar methane flow rate, the visible flame height of the methane–air flame is about three times longer than the methane–oxygen flame at atmospheric conditions. The visible flame heights of methane–air flames, shown in Fig. 2b, essentially stay constant with increasing pressure, which is the same behavior observed in previous studies [24]. However, as shown in Fig. 2a and discussed previously in [21], the visible flame height of methane–oxygen flames decreases as the pressure is increased.

4.2. Measurements of soot volume fraction

The variations in the soot volume fraction with radial location and height above the burner exit for the methane–air flames are compared with the results for the corresponding methane–oxygen flames in Figs. 3 and 4, respectively. At 10 atm, the comparison shows that the maximum soot volume fractions in methane–oxygen

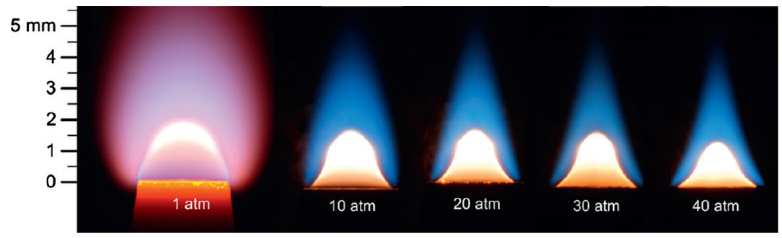

(a) Methane-oxygen

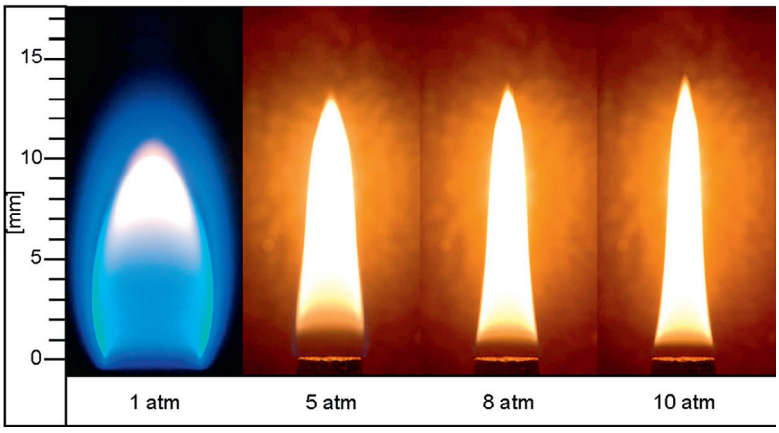

(b) Methane-air

Fig. 2. Still images of (a) methane–oxygen flames from 1 to 40 atm with a methane flow rate of 1.1 mg/s and (b) methane–air flames from 1 to 10 atm with a methane flow rate of 0.825 mg/s. Results for methane–oxygen flames are adopted from [21].

flames are about a factor of three lower than the ones in methane–air flames. It should be noted that this difference would be larger if one considers the fact that the mass flow rate of methane in methane–oxygen flames is about 33% higher than in the methane–air flames. A similar trend is observed when the soot volume fraction profiles for the methane–air and the methane–oxygen flames at 20 atm are compared. The maximum soot volume fractions in methane–air flames are about three times higher than the ones in methane–oxygen flames at 20 atm. At 40 atm, the maximum soot volume fraction in the methane–oxygen flame is about 56 ppm compared to 141 ppm in a similar methane–air flame with half the methane flow rate [24]. In the atmospheric methane–oxygen flame, soot concentrations are very low and not measurable with the current soot diagnostics. Measurements with a line-of-sight attenuation at atmospheric pressure yielded the maximum soot volume fraction much less than 0.1 ppm. It should be noted that the data in Fig. 4 was taken from [21] to facilitate a comparison with the flame-air data shown in Fig. 3.

Overall, Figs. 3 and 4 illustrate that the distribution of soot is similar in both the methane–air and methane–oxygen flames. Soot is distributed in an annular band near the burner rim and this distribution flattens and the peak soot concentrations move towards the flame centerline when pressure is increased.

One of the widely used approaches to assess the sensitivity of soot formation to pressure uses the soot yield, defined as the percentage of total carbon in the fuel converted to soot. The soot yield was suggested to be a better measure than soot volume fraction to assess the influence of pressure on soot formation [27]. As such, this measure was used here and in our previous high pressure studies [22–24]. The mass flow rate of carbon, in the form of soot, can be determined through the relationship

$$\dot{m}_s(z) = 2\pi\rho_s \int v_z(r,z) f_v(r,z) r dr \qquad (1)$$

where v_z is the axial velocity, $\rho_s = 1.8$ g/cm^3 is the soot density, and z is the axial height. The axial velocity may be estimated using the relationship $v_z(z) \approx \sqrt{2az}$, where a is an acceleration constant commonly assumed to be 25 m/s^2 at atmospheric pressure [46]. However, in recent studies [29,31,32] it was found that the acceleration constant a, which is used to estimate the axial velocity of the flame as a function of height, is larger than 25 m/s^2 at super-atmospheric pressures. Based on the calculations performed by Charest et al. [29,31,32], a value of 32 m/s^2 was assumed for the acceleration constant a. A plot of the maximum soot yield as a function of pressure in the methane–oxygen and methane–air flames is shown in Fig. 5. The results for the methane–oxygen flames in [21] were re-evaluated to include the higher buoyancy effects.

As shown in Fig. 5, the methane–air flames produced several times more soot than methane–oxygen flames. In the methane–oxygen flames, soot yield reaches a peak around 40 atm, and then it starts decreasing with further increase in pressure. The soot yield in the methane–air flames reaches a plateau around 40–50 atm, which has also been observed with other other gaseous n-alkane fuels [29]. As noted above, the difference between the soot yields of the methane–air and methane–oxygen flames would be larger if one considered the fact that the mass flow rate of methane in methane–oxygen flames is about 33% higher than in the methane–air flames. Considering the scaling arguments that were discussed in [29]—the soot yield approximately scales with the square root of fuel mass flow rate for diffusion flames burning at or below their smoke points—it is expected that the methane–air soot yield profile shown in Fig. 5 would be approximately 15% higher if the methane flow rate were 1.1 mg/s.

A lack of understanding of the dependence of soot refractive index on soot temperature and the wavelength introduces some degree of uncertainty in the measured soot volume fractions. Nonetheless, the soot refractive index was assumed not to have a

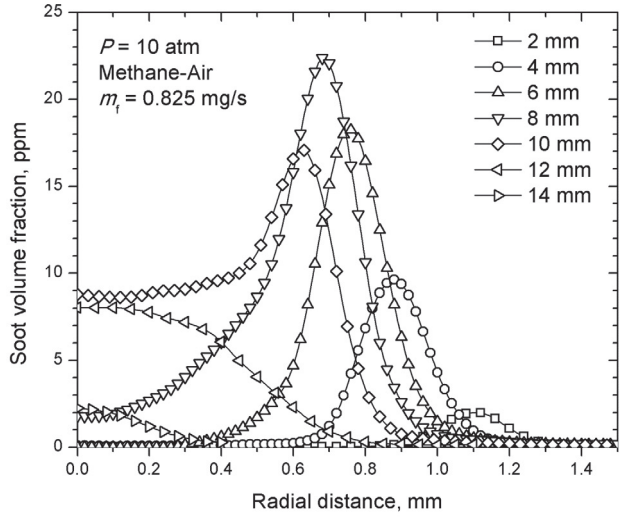

(a) 10 atm

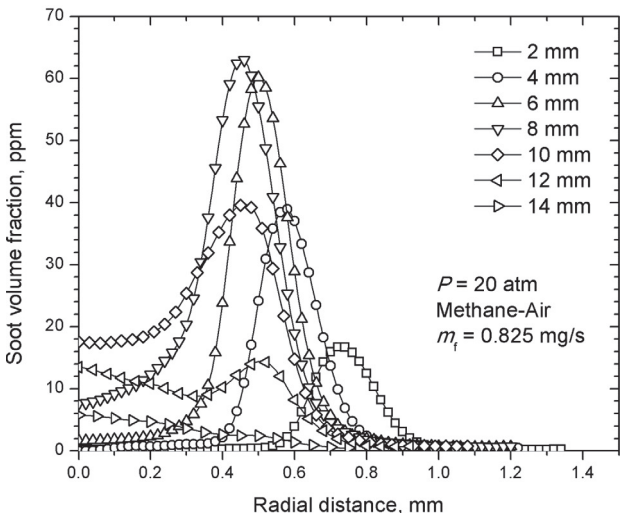

(b) 20 atm

Fig. 3. Radial soot profiles at various heights above the burner exit in the methane–air flames. Methane flow rate is 0.825 mg/s.

significant dependence on temperature or the wavelength. This was necessary to be consistent with previous high-pressure soot measurements [21–23]. Another potential source of uncertainty is the attenuation of emissions by soot in the flames studied here and in [21]. Modeling of the flame emission using the methods described in [26] indicated that the attenuation of soot emissions introduces only a small error into the measurements (i.e., <2%) for even the highest soot loadings encountered in this work. The uncertainty introduced by attenuation is similar to those encountered in atmospheric flames because light attenuation is a function of the product of the soot concentration and the absorption path length. Maximum soot concentrations measured in this study are ten times larger than those observed in similar atmospheric flames, but the flame diameters are much smaller and decrease with increasing pressure. The maximum total uncertainty in soot measurements reported in this work was evaluated as 35%. The error bars in Fig. 5 correspond to this maximum total uncertainty.

4.3. Predictions at 1 atm

The predicted temperature profiles along the flame axis of the methane–oxygen and methane–air flames at one atmosphere are shown in Fig. 6. The corresponding profiles for methane, carbon monoxide, hydrogen, and oxygen mass fraction along the

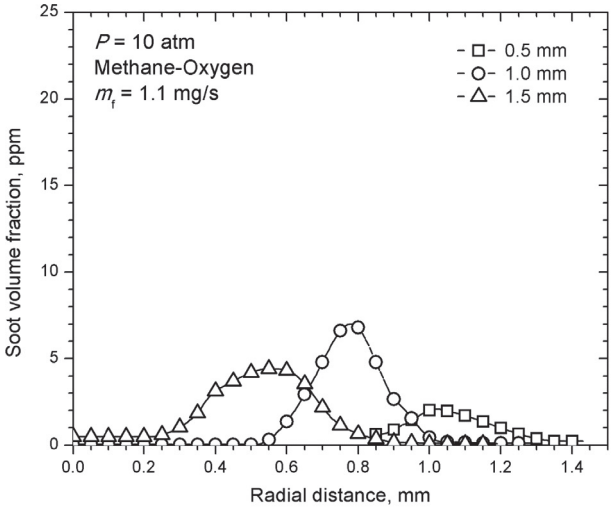

(a) 10 atm

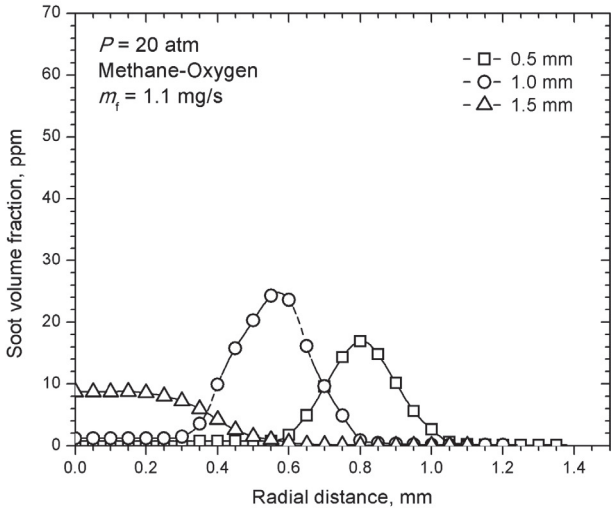

(b) 20 atm

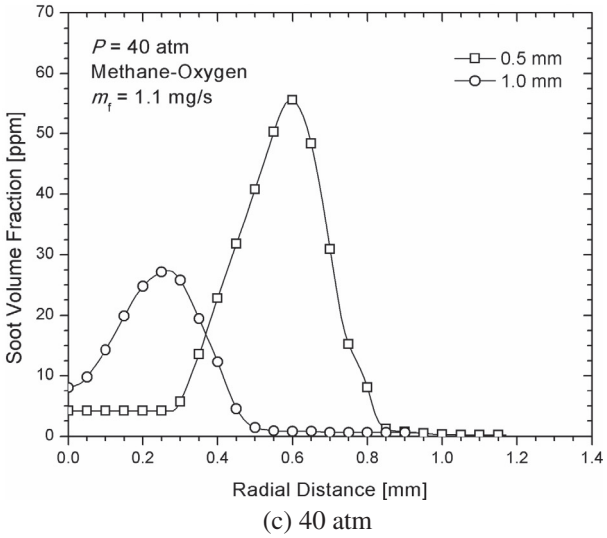

(c) 40 atm

Fig. 4. Radial soot profiles at various heights above the burner exit in the methane–oxygen flames [21]. Methane flow rate is 1.1 mg/s.

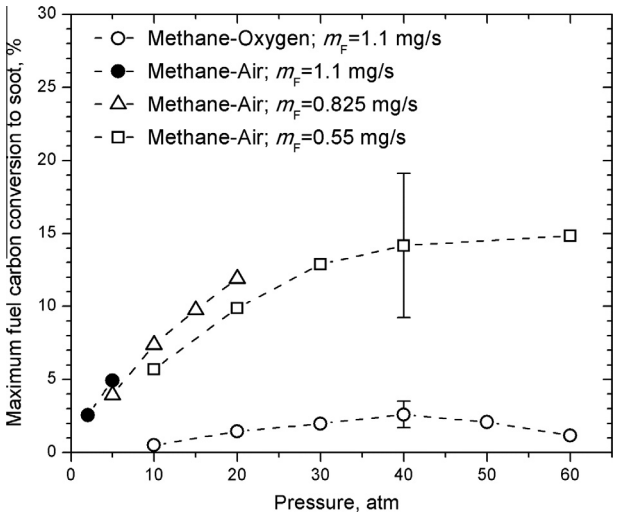

Fig. 5. Maximum soot yields of methane–oxygen and methane–air flames as a function of pressure. Methane–oxygen data in [21] are re-evaluated to include higher buoyancy effects. Methane–air data with the lowest flow rate are from [24].

centerline are also shown in the figure. For the methane–oxygen flames, the locations of the two zones indicated in Fig. 2a were superimposed along the flame axis in Fig. 6. As discussed by Joo and Gülder [21], the maximum centerline temperature of the methane–oxygen flame is about 700–800 K higher than that of methane–air flame. Centerline hydrogen mass fractions along the flame axis indicate that a relatively large amount of hydrogen is produced through the pyrolysis of methane at high temperatures in the methane–oxygen flame, illustrated in Fig. 6. In the methane–oxygen flame, the mass fractions of hydrogen first reach a peak just before the tip of the yellow luminous zone and then hydrogen is depleted by oxygen through a diffusion flame within the blue flame zone. A similar behavior was observed by the mass fraction of carbon monoxide; however, a small portion of carbon monoxide seemed to exit the blue flame tip. As such, Joo and Gülder [21] noted that the blue flame zone is mainly a diffusion flame of hydrogen and carbon monoxide burning in oxygen. But intense penetration of oxygen into the flame causes the flame within the blue zone (zone II) to turn into a partially premixed (stratified) flame downstream; the computed oxygen mass fractions are almost zero at the interface between the two zones and increase with height afterwards. This phenomenon was confirmed herein by plotting the predicted equivalence ratio, Φ, on top of the experimental images of the flame, shown in Fig. 7. The stratified structure with the blue zone is evident.

Figure 8 depicts the predicted mass fractions of small hydrocarbons and radicals along the flame centerline. In zone I of the methane–oxygen flames, intense pyrolysis of methane leads to high concentrations of acetylene, ethylene, and ethane; although these species are mostly destroyed before they reach the tip of the zone I. The blue zone (zone II) contains relatively high concentrations of radicals OH, O, and H radicals as compared to the concentrations in zone I. In the methane–air flames, on the other hand, concentrations of acetylene, ethylene, and ethane are much higher than in methane–oxygen flames while the peak hydrogen and carbon monoxide concentrations are about an order of magnitude lower. Therefore, the preferred pyrolysis products in the methane–air flames are mainly small hydrocarbons, whereas they are small hydrocarbons combined with carbon monoxide and hydrogen for the oxygen-air flames. These differences in species concentrations are primarily the result of the large temperature differences between the two flames.

The predicted temperature contours for both flames are compared in Fig. 9. The location where the mixture fraction is

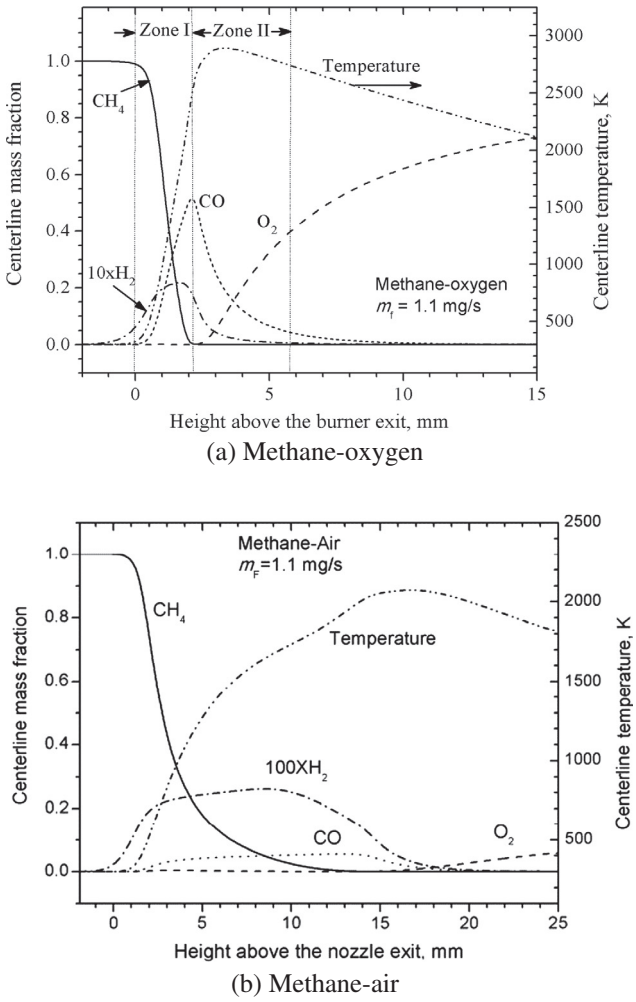

Fig. 6. Predicted temperatures and mass fractions of major species along the flame axis for (a) methane–oxygen and (b) methane–air flames at 1 atm. Methane flow rate is 1.1 mg/s. Horizontal arrows mark the locations of Zone I and Zone II from Fig. 2a. The data was adopted from [21].

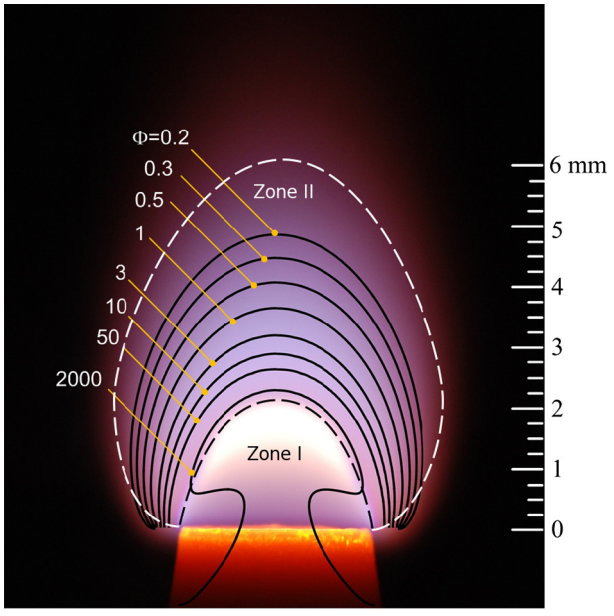

Fig. 7. Predicted equivalence ratios in the methane–oxygen flame at atmospheric pressure. Dashed lines denote the edges of the zones. Methane flow rate is 1.1 mg/s.

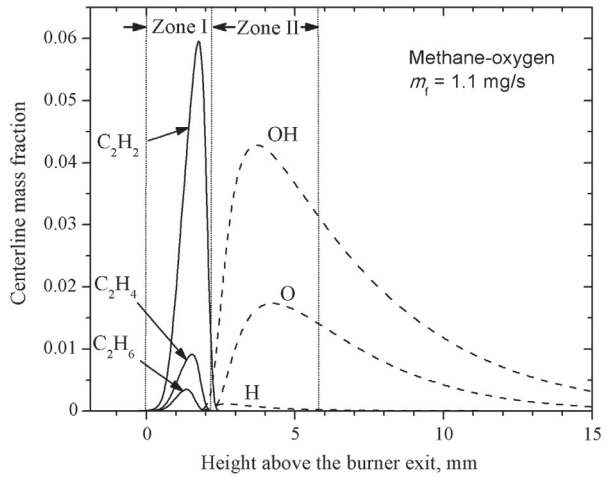

(a) Methane-oxygen

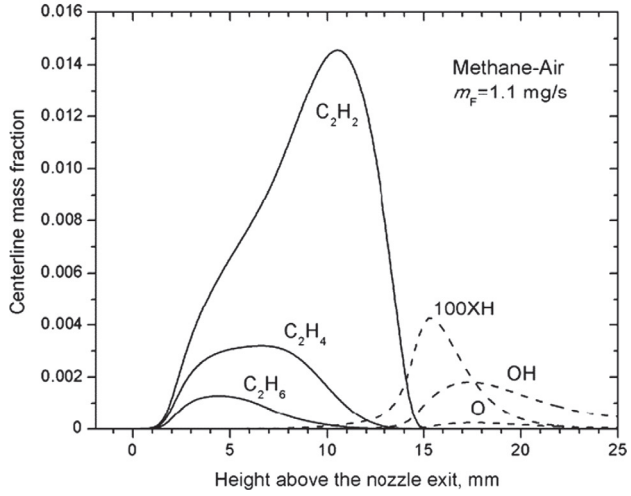

(b) Methane-air

Fig. 8. Predicted mass fractions along the flame axis of acetylene, ethylene, ethane, hydroxyl radical, elemental oxygen and elemental hydrogen for (a) methane–oxygen and (b) methane–air flames at 1 atm. Methane flow rate is 1.1 mg/s. Horizontal arrows mark the locations of Zone I and Zone II from Fig. 2a.

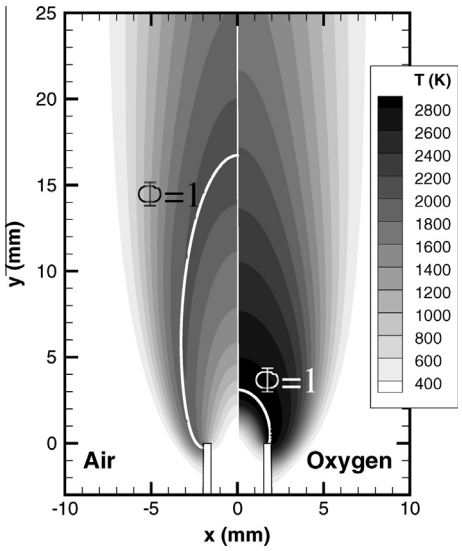

Fig. 9. Predicted temperature contours for methane–air and methane–oxygen flames at 1 atm with a methane mass flow rate of 1.1 mg/s. The solid black lines denote the location where the mixture fraction is equal to the stoichiometric value.

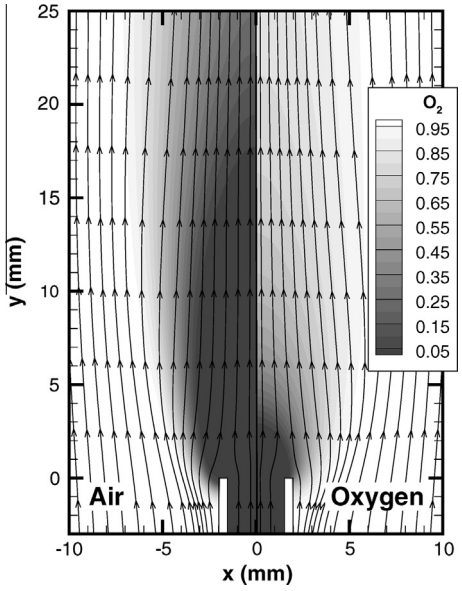

Fig. 10. Predicted contours for oxygen mass fraction in the methane–air and methane–oxygen flames at 1 atm with a methane mass flow rate of 1.1 mg/s. The oxygen mass fraction was normalized by the mass fraction of oxygen in the oxidizer stream. The solid black lines denote the flow streamlines.

stoichiometric is also denoted in the figure. The structure of the two flames is drastically different and peak temperatures occur much lower in the oxygen flame, which corresponds with the results obtained by Joo and Gülder [21]. The predicted peak temperature in the oxygen-air flame is 2910 K, whereas it is only 2072 K in the methane–air flame. This is comparable to the measured peaks of 2075 K and 2600 K for 10 atm methane–air [24] and methane–oxygen flames [21]. Note that the actual temperatures for the 1 atm flames are expected to be slightly higher than the values measured at 10 atm, especially for the methane–oxygen flames. These discrepancies in predicted temperature are largely attributed to the absence of radiation in the numerical model. Additionally, the location of maximum temperature occurs slightly on the lean side of the methane–air flame, but slightly on the rich side of in the oxygen-air flame as also observed by Skeen et al. [46].

Figure 10 shows the fluid streamlines superimposed on the predicted contours for oxygen mass fraction in both flames. Note that the oxygen mass fraction has been normalized by the value in the oxidizer stream, 0.232 for air and 1.0 for oxygen co-flow. Oxygen is able to reach the centerline faster and at a much lower height in the oxygen-air flame. However, the streamlines are not altered significantly by the change in oxidizer. They converge towards the centerline with increasing height faster in the methane–oxygen flame, which is a result of lower densities and stronger buoyant forces since temperatures in the methane–oxygen flame are higher. As such, the higher temperatures—diffusivity increases with temperature—and steeper oxygen concentration gradients in the methane–oxygen flame promote the diffusion of oxygen towards the fuel stream. This results in the high oxygen concentrations along the centerline near the burner and supplies the diffusion flame in zone I with oxidizer.

The effect of oxidizer on the axial flow velocities are presented in Fig. 11. Although the streamlines were not altered significantly, the higher temperatures low in the methane–oxygen flame cause

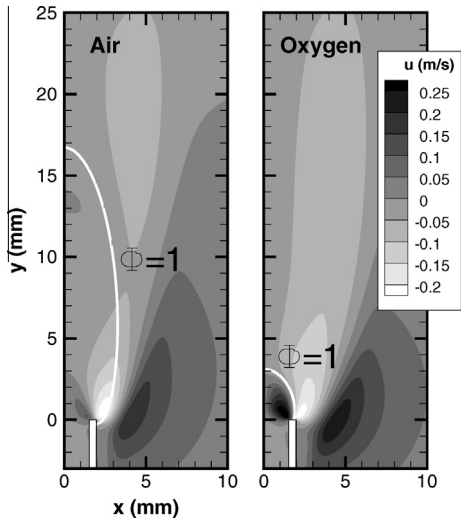

Fig. 11. Predicted axial velocity contours for the methane–air and methane–oxygen flames at 1 atm with a methane mass flow rate of 1.1 mg/s. The solid black lines denote the location where the mixture fraction is equal to the stoichiometric value.

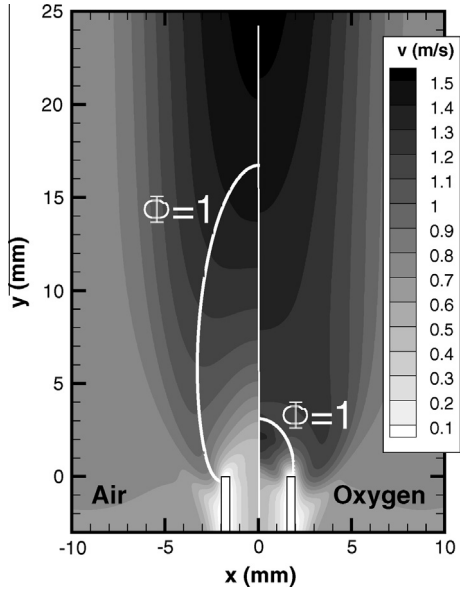

Fig. 12. Predicted radial velocity contours for the methane–air and methane–oxygen flames at 1 atm with a methane mass flow rate of 1.1 mg/s. The solid black lines denote the location where the mixture fraction is equal to the stoichiometric value.

the flow to accelerate much faster. Higher up in the flame, the axial velocities of the two flames are similar. Interestingly, there is a region of gas in the methane–oxygen flame with a high upward velocity near the burner exit plane along the centerline. This indicates that the flow near the axis accelerates quickly, slows down across the flame front, and then speeds up once again. This decrease is caused by the diffusion of oxygen towards the flame, against the upward velocity of the bulk flow. Contours of the radial velocity, Fig. 12 shows a similar increase in velocity of the fuel stream towards the oxidizer when oxygen is used for the co-flow. As such, mass transport intensifies due to the higher temperatures and concentration gradients in the pure oxygen flame. The higher upward velocities in the lower portion of the pure oxygen flame are also expected to enhance the entrainment of oxidizer into the core flow.

5. Concluding remarks

Through further experimental and numerical analysis, the structure and characteristics of laminar methane–oxygen diffusion flames were compared with those of similar methane–air flames. The distinct two-zone structure originally reported by Joo and Gülder [21] was observed in the methane–oxygen flames that persisted over the range of pressures investigated (1–60 atm). The inner zone has a yellow/orange colour, similar to hydrocarbon-air flames, and is surrounded by a larger blue outer zone. Methane–air diffusion flames had a thin layer of blue outer zone at atmospheric pressure; however, this zone completely disappeared when the pressure was increased above atmospheric. Maximum soot yields of methane–air flames were consistently higher than methane–oxygen flames at all pressures. The soot yield of the methane–oxygen flames reached a peak at about 40 atm and then started decreasing as the pressure further increased, whereas the soot yield of the methane–air flames reached a plateau at about 40 atm and did not change much with further pressure increase.

The distinct two-zone structure of the methane–oxygen flames was not observed when air was used as the co-flow oxidizer. Numerical simulations showed that when pure oxygen was used in the co-flow stream, a relatively large amount of hydrogen and carbon monoxide was produced in the inner zone from high temperature pyrolysis of the fuel. This early fuel pyrolysis was confirmed by the significant amounts acetylene, ethylene, and ethane produced and destroyed within the inner zone. The outer zone of the methane–oxygen flames had a stratified structure with a very steep equivalence ratio gradient. The main reactions in this outer zone are the oxidation of the hydrogen and carbon monoxide that was produced within the inner zone.

The presence of the two-zone structure in the methane–oxygen flames was attributed to the intensified penetration of oxygen into the core flow. The higher diffusivities, steeper oxygen concentration gradients, and enhanced entrainment increase the transport of oxygen to the flame. As such, there is sufficient oxygen present near the base of the flame to support the diffusion flame in the inner zone of the methane–oxygen flames. Overall, mass transfer rates are higher when pure oxygen is used instead of air for the co-flow stream because of the higher temperatures, steeper concentration gradients, and stronger buoyancy forces. The abundance of oxygen near the centerline, even in the lower portion of the flame, also promotes the oxidation of soot.

Acknowledgments

We thank G. Intasopa with the help he provided with the experimental work. We acknowledge an infrastructure grant provided by Canada Foundation for Innovation for building the high pressure combustion vessel and associated components as well as acquiring the diagnostic equipment. Operational funds for this work have been provided by the Natural Sciences and Engineering Research Council and the Canadian Space Agency. Computational resources for performing all of the calculations reported herein were provided by the SciNet High Performance Computing Consortium at the University of Toronto and Compute/Calcul Canada through funding from the Canada Foundation for Innovation and the Province of Ontario, Canada.

References

[1] H.F. Calcote, D.M. Manos, Combust. Flame 49 (1983) 289–304.
[2] D.B. Olson, J.C. Pickens, R.J. Gill, Combust. Flame 62 (1985) 43–60.
[3] J.H. Kent, Combust. Flame 63 (1986) 349–358.
[4] B.S. Haynes, H. Gg, Wagner, Prog. Energy Combust. Sci. 7 (1981) 229–273.
[5] Ö.L. Gülder, Combust. Flame 78 (1989) 179–194.
[6] Ö.L. Gülder, D.R. Snelling, Combust. Flame 92 (1993) 115–124.

[7] G. Sugiyama, Proc. Combust. Inst. 25 (1994) 601–608.
[8] K.-O. Lee, C.M. Megaridis, S. Zelepouga, A.V. Savaliev, L.A. Kennedy, O. Charon, S. Ammouri, Combust. Flame 121 (2000) 323–333.
[9] D.X. Du, R.L. Axelbaum, C.K. Law, Proc. Combust. Inst. 23 (1990) 1501–1507.
[10] Ö.L. Gülder, Combust. Flame 101 (1995) 302–310.
[11] R.L. Schalla, G.E. McDonald, Proc. Combust. Inst. 5 (1955) 316–324.
[12] R.L. Schalla, G.E. McDonald, Formation and Combustion of Smoke in Laminar Flames, Tech. Rep. 1186, NACA, 1954.
[13] A.E. Karatas, Ö.L. Gülder, Prog. Energy Combust. Sci. 38 (2012) 818–845.
[14] S.K. Choi, J. Kim, S.H. Chung, J.S. Kim, Combust. Theory Model. 13 (1) (2009) 39–56.
[15] K. Bhadraiah, V. Raghavan, Combust. Theory Model. 15 (1) (2011) 23–46.
[16] C.Y. Liu, G. Chen, N. Sipöcz, M. Assadi, X.S. Bai, Appl. Energy 89 (2012) 387–394.
[17] J. Lux, O. Haidn, AIAA J. Propul. Power 25 (2009) 15–23.
[18] L. Pons, N. Darabiha, S. Candel, G. Ribert, V. Yang, Combust. Theory Model. 13 (2009) 57–81.
[19] N. Zong, V. Yang, Proc. Combust. Inst. 31 (2007) 2309–2317.
[20] B.A. Palyonov, A.I. Bessonov, A.I. Pastuhov, S.S. Shulkova, G.P. Kalmykov, in: C. Bruno, A.G. Accettura (Eds.), Advanced Propulsion Systems and Technologies, Today to 2020, vol. 23, AIAA Progress in Aeronautics and Astronautics, 2008, pp. 163–171.
[21] H.I. Joo, Ö.L. Gülder, Combust. Flame 157 (2010) 1194–1201.
[22] K.A. Thomson, O.L. Gülder, E.J. Weckman, R.A. Fraser, G.J. Smallwood, D.R. Snelling, Combust. Flame 140 (2005) 222–232.
[23] D.S. Bento, K.A. Thomson, O.L. Gülder, Combust. Flame 145 (2006) 765–778.
[24] H.I. Joo, O.L. Gülder, Proc. Combust. Inst. 22 (2009) 769–775.
[25] C.J. Dasch, App. Opt. 31 (8) (1992) 1146–1152.
[26] D.R. Snelling, K.A. Thomson, G.J. Smallwood, O.L. Gülder, E.J. Weckman, R.A. Fraser, AIAA J. 40 (9) (2002) 1789–1795.
[27] W.L. Flower, C.T. Bowman, Proc. Combust. Inst. 21 (1988) 1115–1124.
[28] R.W. Davis, E.F. Moore, R.J. Santoro, J.R. Ness, Combust. Sci. Technol. 73 (1990) 625–635.
[29] Ö.L. Gülder, G. Intasopa, H.I. Joo, P.M. Mandatori, D.S. Bento, M.E. Vaillancourt, Combust. Flame 158 (2011) 2037–2044.
[30] M.R.J. Charest, C.P.T. Groth, Ö.L. Gülder, Combust. Theory Model. 14 (2010) 793–825.
[31] M.R.J. Charest, H.I. Joo, Ö.L. Gülder, C.P.T. Groth, Proc. Combust. Inst. 33 (2011) 549–557.
[32] M.R.J. Charest, Ö.L. Gülder, C.P.T. Groth, Combust. Flame 158 (2011) 860–875.
[33] M.R.J. Charest, Ö.L. Gülder, C.P.T. Groth, Combust. Flame 158 (2011) 1933–1945.
[34] K.K. Kuo, Principles of Combustion, second ed., John Wiley & Sons, Inc., New Jersey, 2005.
[35] J.S. Sachdev, C.P.T. Groth, J.J. Gottlieb, Int. J. Comput. Fluid Dyn. 19 (2005) 157–175.
[36] S.A. Northrup, C.P.T. Groth, AIAA Paper 2005–0547, January, 2005.
[37] S.A. Northrup, C.P.T. Groth, Solution of laminar combusting flows using a parallel implicit adaptive mesh refinement algorithm, in: Proceedings of the Fourth International Conference on Computational Fluid Dynamics, ICCFD4, Ghent, Belgium, 2006. pp. 341–346.
[38] X. Gao, C.P.T. Groth, Int. J. Comput. Fluid Dyn. 20 (2006) 349–357.
[39] X. Gao, S.A. Northrup, C.P.T. Groth, Prog. Comput. Fluid Dyn. 11 (2011) 76–95.
[40] P.L. Roe, J. Comput. Phys. 43 (1981) 357–372.
[41] W.J. Coirier, K.G. Powell, AIAA J. 34 (1996) 938–945.
[42] J.M. Weiss, W.A. Smith, AIAA J. 33 (1995) 2050–2057.
[43] D.G. Goodwin, Chem. Vap. Deposition XVI and EUROCVD 14 (2003) 155–162.
[44] G.P. Smith, D.M. Golden, M. Frenklach, N.W. Moriarty, B. Eiteneer, M. Goldenberg, C.T. Bowman, R.K. Hanson, S. Song, W.C. Gardiner, Jr., V.V. Lissianski, Z. Qin, Gri-mech 3.0, 2002, <http://www.me.berkeley.edu/gri_mech/>.
[45] K. Saito, F.A. Williams, A.S. Gordon, Combust. Sci. Technol. 47 (1986) 117–138.
[46] S.A. Skeen, G. Yablonsky, R.L. Axelbaum, Combust. Flame 156 (2009) 2145–2152.